atmosphere

MDPI

Article

Characterizing and Removing Ultra-Violet Contamination in Ion Observations on Board Tianwen-1

Limin Wang [1,2,3,4], Lei Li [1,2,3,*], Wenya Li [1,2,3], Linggao Kong [1,5,6], Binbin Tang [1,2,3], Jijie Ma [1,4,5], Yiteng Zhang [1,2,3], Lianghai Xie [1,2,3], Aibing Zhang [1,4,5], Fuhao Qiao [1,2,3,4], Peter Wurz [7] and André Galli [7]

1 National Space Science Center, Chinese Academy of Sciences, Beijing 100190, China; wanglimin19@mails.ucas.ac.cn (L.W.); wyli@spaceweather.ac.cn (W.L.); lgkong@nju.edu.cn (L.K.); bbtang@spaceweather.ac.cn (B.T.); majijie19@mails.ucas.ac.cn (J.M.); ytzhang@nssc.ac.cn (Y.Z.); xielianghai@nssc.ac.cn (L.X.); zhab@nssc.ac.cn (A.Z.); qiaofuhao19@mails.ucas.ac.cn (F.Q.)
2 State Key Laboratory of Space Weather, National Space Science Center, Chinese Academy of Sciences, Beijing 100190, China
3 Key Laboratory of Solar Activity and Space Weather, National Space Science Center, Chinese Academy of Sciences, Beijing 100190, China
4 University of Chinese Academy of Sciences, Beijing 100049, China
5 Beijing Key Laboratory of Space Environment Exploration, Beijing 100190, China
6 Institute of Science and Technology for Deep Space Exploration, Suzhou Campus, Nanjing University, Suzhou 215163, China
7 Space Research and Planetary Sciences, Physics Institute, University of Bern, 3012 Bern, Switzerland; peter.wurz@space.unibe.ch (P.W.); andre.galli@unibe.ch (A.G.)
* Correspondence: lil@nssc.ac.cn

Abstract: The Mars Ion and Neutral Particle Analyzer (MINPA) onboard Tianwen-1 aims to study the interaction between Mars and the solar wind via in situ ion measurement and energetic neutral atom imaging. Despite the efforts for Ultra-Violet suppression in MINPA design, 0.48% of ion observations from November 2021 to July 2022 were identified as UV-contaminated. The UV emissions primarily penetrate into the instrument through the ENA entrance. Statistically, the distribution of the UV contamination in phase space typically spans 3 to 4 azimuth sectors. The contamination is uniformly distributed across the polar dimension while, in the energy and mass dimensions, it is proportional to the time-of-flight duration. Comparisons between the in-flight performance and ground calibration suggest that azimuthal broadening and intensity variations of the contamination may result from differing responses across the azimuthal sectors. Based on the characteristics of the UV impact on MINPA ion observations, a removal algorithm is proposed to reduce contamination while preserving valid signals, which improves the data quality effectively and benefits the interpretation of MINPA's ion measurements in the Martian space environment. The cause, effect, and distribution of the UV contamination obtained by this study may serve as a reference for other space ion observations.

Keywords: ion observations; UV contamination; electrostatic analyzer; Tianwen-1

Citation: Wang, L.; Li, L.; Li, W.; Kong, L.; Tang, B.; Ma, J.; Zhang, Y.; Xie, L.; Zhang, A.; Qiao, F.; et al. Characterizing and Removing Ultra-Violet Contamination in Ion Observations on Board Tianwen-1. *Atmosphere* **2024**, *15*, 19. https://doi.org/10.3390/atmos15010019

Academic Editor: Leonardo Primavera

Received: 23 November 2023
Revised: 18 December 2023
Accepted: 20 December 2023
Published: 23 December 2023

1. Introduction

Particle detection, which includes measurements of charged and neutral particles, plays a crucial role in the exploration of planets. Without shelter from the intrinsic magnetic field [1,2], the atmospheres of unmagnetized planets, such as Mars, are susceptible to erosion by the solar wind after ionization by the solar extreme Ultra-Violet (EUV) emissions [3–5]. Detection of plasma and energetic neutral atoms (ENAs) produced through charge exchange collisions between the upper atmosphere and the plasma [6–8] enables monitoring of atmospheric escape and enhances our understanding of the evolution of planetary habitability. Electro Static Analyzer (ESA), the most common detector for

charged particles, is widely utilized in interplanetary, terrestrial, and planetary exploration missions, e.g., Advanced Composition Explorer (ACE), Cluster, and Mars Atmosphere and Volatile Evolution (MAVEN) [9–12].

Like the pioneer Chinese Mars exploration mission, Tianwen-1, comprising an orbiter and the Zhurong rover, aims to investigate various aspects of Mars, including the Martian topography and geological structure, the material composition of Mars' surface, and the distribution of water-ice, the magnetosphere, ionosphere and their interaction with the solar wind, the Martian gravity field and its interior structure [13]. The Mars Ion and Neutral Particle Analyzer (MINPA) onboard Tianwen-1 is designed to investigate the interaction between the solar wind and the Mars atmosphere [14]. MINPA employs a standard toroidal top-hat electrostatic analyzer with a time-of-flight (TOF) mass analyzer to detect ions in situ and image plasma remotely through ENAs. Notably, MINPA introduces an innovative design to integrate the ion and ENA detection units into a single sensor head. The instrument sensors alternately receive ions from outer space and ions generated by ENAs hitting the charge exchange plate by manipulating the voltages at the entrances for ions and ENAs. Then, ESA selects incident particles of specific energy-to-charge ratios by deflecting them with an electrostatic field applied between concentric plates [15–18]. The TOF mass analyzer determines the mass-to-charge ratio of ions by measuring the time for particles to travel a fixed distance [19]. Discrete anodes resolve the azimuthal direction of the ion's velocity, while the measurement of velocity outside the intrinsic planer field of view is accomplished by the electrostatic deflectors positioned at the front entrance. These designs enable MINPA to resolve velocity for the main ion and ENA species. More detailed information about MINPA can be found in the instrument article [14].

However, the micro-channel plates (MCPs) used for amplifying electronic signals are extremely sensitive to the solar Ultra-Violet (UV) emissions, particularly the Lyman α emission at 121.6 nm [20,21], which is both energetic (10.2 eV) and intense in the vicinity of Mars (~2.6 mW/m^2) [22]. These emissions, as well as their secondary photoelectrons, hit the MCP, introducing significant noise [21]. Since the voltages used to deflect ions make it difficult for photoelectrons to access the MCP, direct impact by photons may be the primary contributing factor. Given that photons are not influenced by the electrostatic field, the UV emission generally contaminates all energy, mass, and polar angle channels and partial azimuthal angle, which is a prevalent issue for ESA in-flight operations. To suppress UV contamination, light baffles, light traps, and low-reflectivity diffuse coatings are frequently incorporated into the design of ESAs [21]. Careful designs of spacecraft orbits and instrument attitudes are also essential to prevent direct exposure of particle entrances to the sunlight. Additionally, various data processing routines are devised to minimize the effects of UV emissions. For instance, in the data process of the ASPERA-3 Ion Mass Analyzer (IMA) on the Mars Express (MEX) mission, Fränz et al. [23] recommended subtracting the maximum count rate of each angular sector with energy more than 8 keV and less than 40 eV from all bins for most UV-contamination scenarios. In the case of severe UV contamination, the mean counts of non-zero bins were subtracted from all bins. Similarly, Nozzoli and Richelli utilized the data where the solar wind was beyond the field-of-view (FOV), yet the UV contamination was detected to evaluate and remove the UV effect [24]. These methods observably reduced the noise level.

MINPA coated its ion and ENA entrance paths and the outer surface of the ESA internal sphere to suppress UV contamination. Ground calibration shows that MINPA achieved a very high UV suppressing efficiency (>98%) [14]. However, UV-contamination has already been found in the in-flight ion and ENA measurements. To access the UV effects on MINPA ion observations and provide an adequate explanation of the ion data, this work analyzes the UV contamination in the MINPA ion observations from November 2021 to July 2022.

2. In-Flight Operation of Tianwen-1 and MINPA

The journey of Tianwen-1 began with its launch on 23 July, 2020, followed by a seven-month cruise phase to Mars. During the cruise phase, MINPA operated for approximately three months, demonstrating good in-flight performance [25–27]. After it successfully entered an orbit around Mars, MINPA commenced regular scientific data collection following an elliptical orbit of 243 km × 10,760 km from November 2021. Figure 1a–c illustrate the Tianwen-1 orbiter and MINPA in the spacecraft coordinates (X_b, Y_b, Z_b). As shown in Figure 1a, MINPA is mounted on the spacecraft main deck, in the $+X_b$ plane, close to the $+Z_b$ corner, but slightly shifted by 6.23° toward the $+Y_b$ side. The ion FOV of MINPA covers the entire 2π $+X_b$ hemisphere. Figure 1a also defines two angles: the solar incident angle (α_{Sun}) and the solar azimuth angle (β_{Sun}). α_{Sun} is the angle between the sunward direction (indicated by the green arrowed line) and $+X_b$, ranging from 0° to 180°. In the Y_b–Z_b plane, β_{Sun} is defined as the anti-clockwise angle from the $-Y_b$ axis to the projected sunward direction, ranging from 0° to 360°. As shown in Figure 1b,c, MINPA has 16 polar sectors covering the instrument polar angle (θ: 0°–90°), and 16 azimuth sectors covering the instrument azimuth angle (φ: 0°–360°). The ENA window, located in the equatorial plane of MINPA, has a field of view of 9.7° × 360° with an angular resolution of 9.7° × 22.5°.

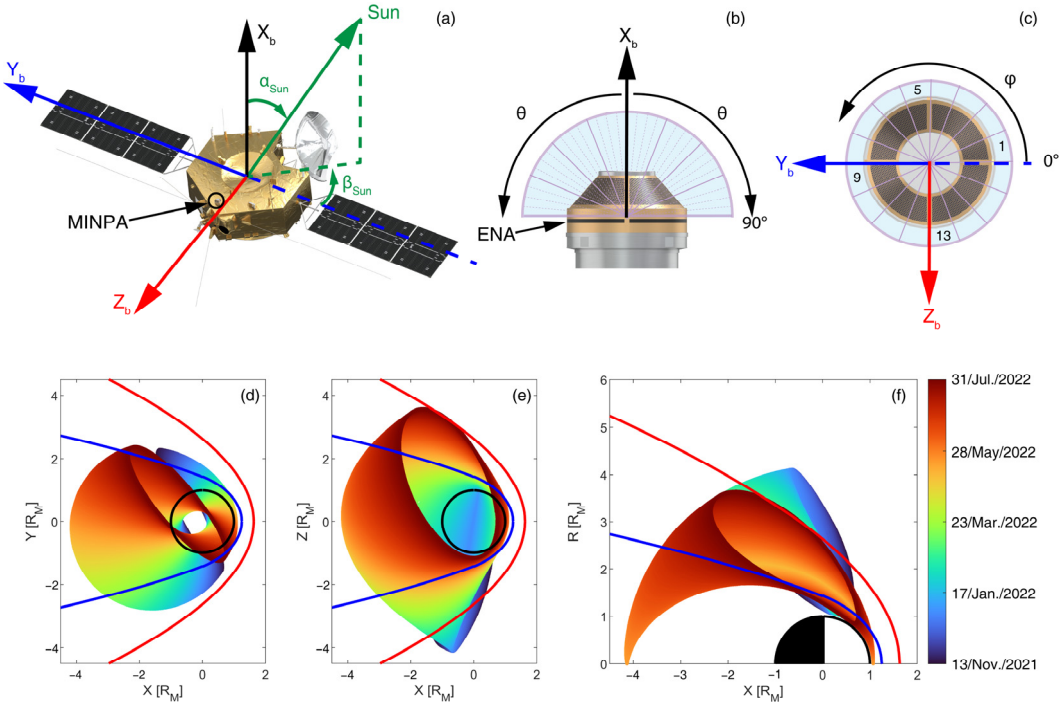

Figure 1. Tianwen-1 orbiter, MINPA, and the orbits. (**a**) Tianwen-1 orbiter and the illustrations of the solar incident angle (α_{Sun}) and solar azimuth angle (β_{Sun}) relative to the spacecraft coordinates (X_b, Y_b, Z_b). MINPA is mounted on the $+Z_b$ corner. (**b**) Side and (**c**) top views of MINPA, with the illustrations of the instrument polar (θ) and azimuthal (φ) angles. (**d**–**f**) Tianwen-1 orbits from 13 November 2021 to 31 July 2022 in the Mars-Sun-Orbital (MSO) coordinate system. R_M is the radius of Mars. The red and blue curves in (**d**–**f**) represent the nominal bow shock and magnetic pileup boundary (MPB), respectively [28].

Figure 1d–f show the Tianwen-1 orbits spanning from 13 November 2021 to 31 July 2022 in the Mars-Sun-Orbit (MSO) coordinate system, where the X_{MSO} axis points from Mars toward the Sun, the Z_{MSO} axis aligns with the normal of Mars' orbital plane, and the Y_{MSO} axis completes the right-handed system. The orbital period of Tianwen-1 is approximately 7.1 h. Throughout the presented time interval, the orbital apoapsis gradually shifted from the southern to the northern poles. As shown in Figure 2, the Tianwen-1 orbiter utilizes two different attitude references: the Sun-oriented and the Mars-oriented

references. In the Sun-oriented reference $+X_b$,$+Y_b$, and $+Z_b$ are aligned with $-Y_{MSO}$, $+Z_{MSO}$, and $-X_{MSO}$, respectively. The Mars-oriented reference has $+Z_b$ pointing toward the center of Mars, $+X_b$ perpendicular to the line connecting Mars and the spacecraft and making an angle less than 90° with the direction of the spacecraft's orbital motion, and $+Y_b$ completing the right-handed system. Tianwen-1 switches between these two attitudes approximately every three orbits, as indicated by the inner colored ellipse in Figure 2. During the apoapsis segment, Tianwen-1 adopts the Sun-oriented attitude (green), and the ion FOV covers the $-Y_{MSO}$ hemisphere. In the periapsis segment, Tianwen-1 switches to the Mars-oriented attitude (red) to capture the cold planetary ions in the windward direction. Between these two attitudes, Tianwen-1 performs maneuvers (black). In the following two orbits, Tianwen-1 will maintain the Sun-oriented attitude. However, if there are special scientific assignments, Tianwen-1 will contingently adjust its attitude. Figure 2 also presents the operational modes of MINPA ion observations by the outer colored ellipse. MINPA works in three modes with ion data products binned in varying mass(M), energy(E), phi(P), and theta (T) resolutions: the default mode (8M×40E×16P×4T), the magnetotail mode (8M×64E×16P×4T), and the ionosphere mode (32M×48E).

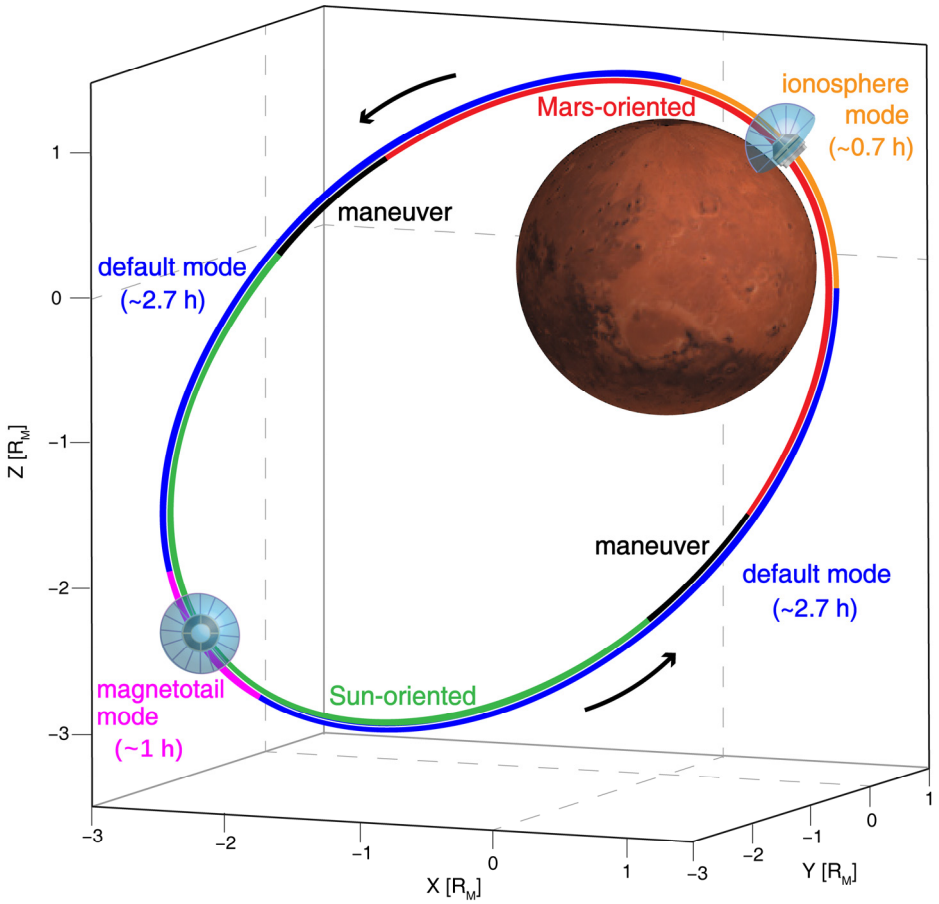

Figure 2. Schematic of Tianwen-1 attitude references and MINPA operation modes. MINPA ion FOVs in the Sun-oriented and Mars-oriented attitudes are also given. The ellipse is a Tianwen-1 orbit in the MSO coordinate system. The inner colors represent the attitude references of Tianwen-1 during its regular operation phase. In the apoapsis segment (green), Tianwen-1 is in the Sun-oriented attitude ($-Z_b$ points toward the Sun). In the periapsis segment (red), Tianwen-1 is in the Mars-oriented attitude ($+Z_b$ points toward the Mars). The black curves show the Tianwen-1 maneuver phases. The outer colored curves represent three MINPA operation modes: default (blue), ionosphere (orange), and magnetotail (magenta) modes.

3. Contamination Caused by the Solar UV Light

3.1. An Example of the UV Contamination

Figure 3 presents an example of the MINPA ion observations in the magnetosheath along an inbound orbit from 15:20 UT to 16:30 UT on 09 December 2021. The corresponding Tianwen-1 orbit for this interval is presented in Figure 3a–c. The spacecraft was initially in the magnetosheath near the bow shock and moved toward the magnetic pileup boundary (MPB). Figure 3d illustrates the time series of the solar incident angle (α_{Sun}) and the solar azimuth angle (β_{Sun}). The green bar at the top of Figure 3d and the green orbits in Figure 3a–c indicate that the Tianwen-1 orbiter adopted the Sun-oriented attitude from 15:20 UT to 15:32 UT. During this period, both α_{Sun} and β_{Sun} remained stable at 90° (Figure 3d). Thereafter, the orbiter maneuvered, gradually from the Sun-oriented attitude to the Mars-oriented attitude, as denoted by the black bar and black orbit arcs. In the early phase of the maneuver, α_{Sun} rapidly decreased to 57° and then increased back to 88°, while the spacecraft rotated anti-clockwise, resulting in a final β_{Sun} value of 345°. Afterward, α_{Sun} decreased slowly to 87.5°, and β_{Sun} increased to 346°. From 16:01 UT onward, the attitude remained Mars-oriented, accompanied by a further decrease in α_{Sun} and a gradual increase in β_{Sun}.

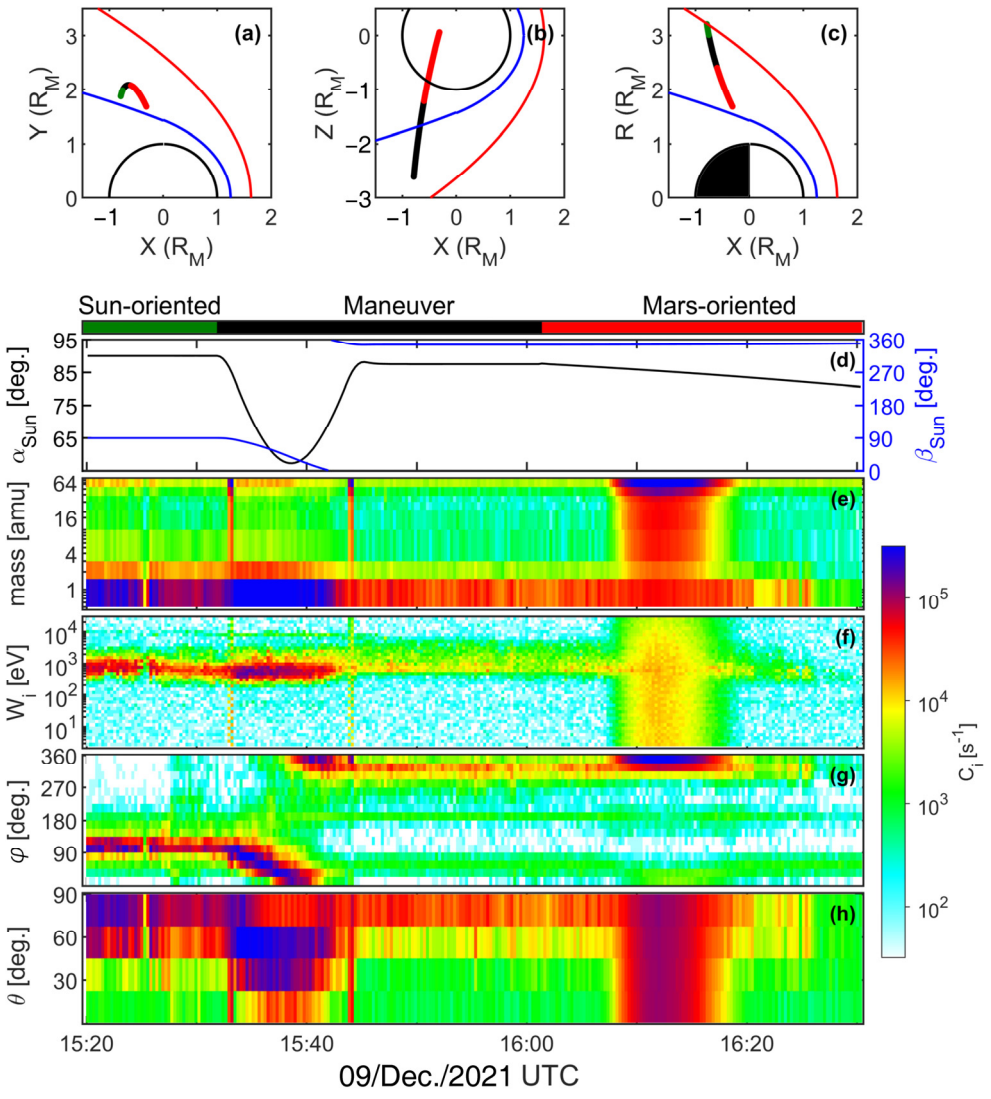

Figure 3. Time series of MINPA ion measurement on 09 December 2021 from 15:20 to 16:30 UT. (**a**–**c**) Tianwen-1 orbits in MSO. The red and blue curves are the nominal bow shock and MPB, respectively. (**d**) Solar incident angle (α_{Sun}) and solar azimuth angle (β_{Sun}). Ion count-rate spectrograms

with respect to (**e**) ion mass, (**f**) energy (W_i), (**g**) azimuth angle (φ), and (**h**) polar angle (θ). Ion mass between 1 and 60 amu (the first 7 mass channels) are counted in (**f**–**h**). The colored orbits in (**a**–**c**) and the colored bars on top of (**d**) show the spacecraft attitudes (green: Sun-oriented, black: maneuver, red: Mars-oriented).

Figure 3e presents the mass spectrogram of the ion count rate (C_i), and Figure 3f–h display the energy, polar, and azimuth angular spectrograms of the total ion count rate for masses below 60 amu (the first 7 mass channels), respectively. In this event, MINPA detected shocked solar wind H^+ and He^{2+} ions, as well as pick-up heavy ions of Mars ionosphere origin, appearing above the magnetosheath ions between 15:20 UT and 16:10 UT. During the maneuver, the observed flow direction of the magnetosheath ions continuously changed with the solar incident angle α_{Sun} and the solar azimuth angle β_{Sun}. The reduced ion count rate after the maneuver is likely due to the limitation of the FOV. In the Mars-oriented phase, MINPA's $+X_b$ axis is perpendicular to the Mars-orbiter line, resulting in an FOV unfavorable for the magnetosheath measurements. As illustrated by the spectrograms in Figure 3e–h, the MINPA ion observations exhibit two types of contamination. The first type is characterized by high count rate noise distributed almost uniformly across all ion masses, energies, and polar angles, within a certain range of azimuthal angle. Examples of this type can be observed at 15:33 UT and 15:44 UT during the maneuver, as well as from 16:07 UT to 16:18 UT during the Mars-oriented phase in Figure 3. These contaminations are likely caused by the solar UV emission [23]. The second type of contamination featured ubiquitous low-count rate random noise across all energies. The noise could be generated by radioactive decay in the MCP glass, and/or the cosmic rays [18,24]. In this report, we focus on the high count-rate contamination.

The ions in the Mars space environment consist of those originating from the solar wind, primarily H^+ and He^{2+} ions, and the Martian ionosphere, mainly O^+, O_2^+ and CO_2^+ ions, as well as ionized exospheric neutral particles, predominantly H^+ ions. It is important to note that ions with masses exceeding 60 amu are rare in the Mars space environment. Therefore, the signals detected by the heaviest mass channel (ranging from 60 amu to 70 amu) are reasonably considered as noise accumulated over the longest TOF duration, and they can be used to identify and quantify the UV contamination. Figure 4a–c present the ion count-rate spectrograms for the heaviest mass channel of MINPA. The high count-rate contaminations are easily distinguished as two narrow stripes and one wide stripe covering all energy channels (Figure 4a) and polar angles (Figure 4c). Figure 4b illustrates that a strong correlation between these contaminations and the Sun-pointing direction (β_{Sun}), denoted by the black curve. Additionally, it could be noted in Figure 4a that ions with the same energy (~1 keV) as the aforementioned magnetosheath ion populations are ghost peaks, caused by the internal scattering of protons, and they are commonly observed by other ion instruments as well [18,29].

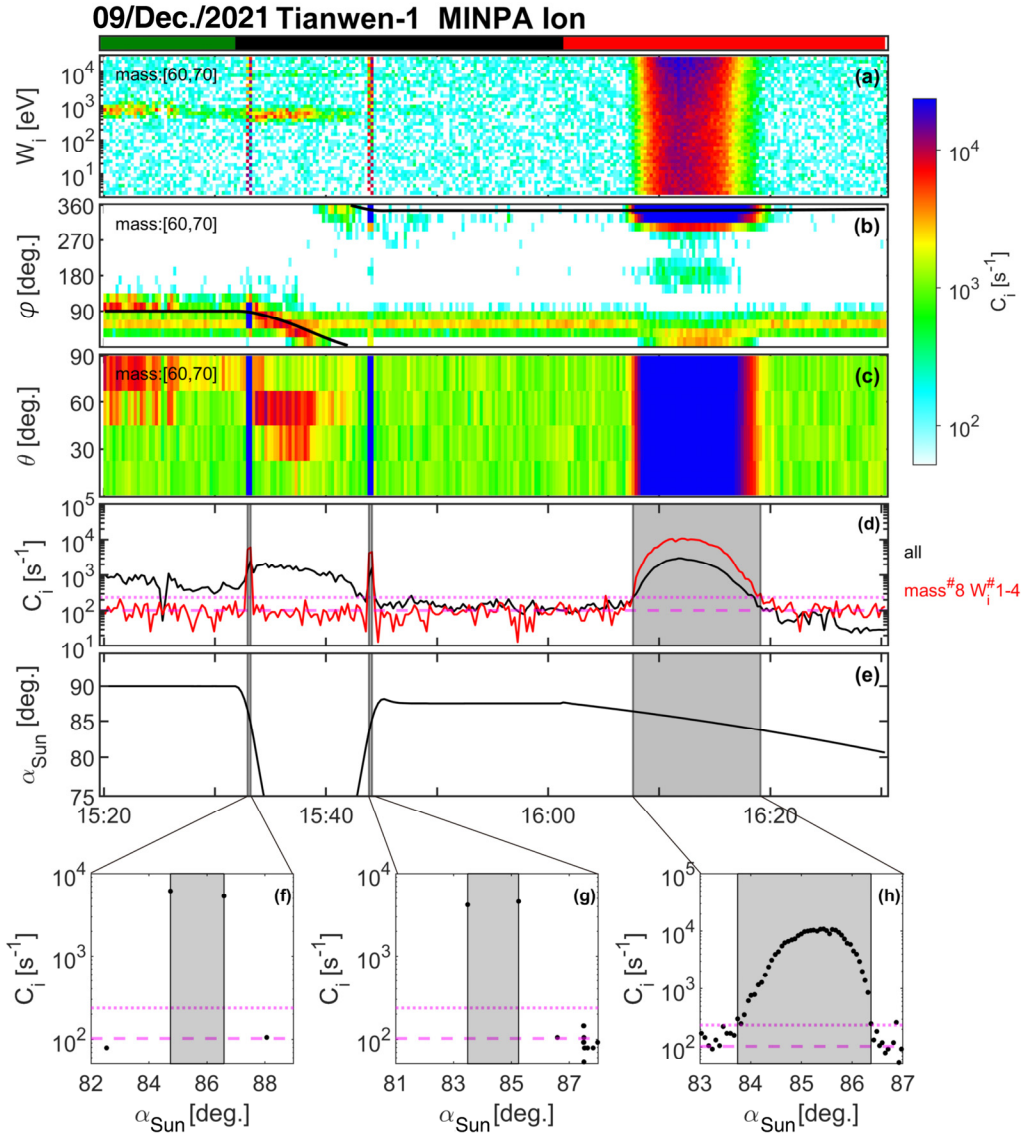

Figure 4. Count-rate spectrograms with respect to (**a**) W_i, (**b**) φ and (**c**) θ for ion mass between 60 and 70 amu (the last mass channel). (**d**) The red curve shows the direction-integrated and energy-averaged count rate for the 8th mass channel between 2.5 eV to 6.36 eV (the first four energy channels), and the black curve gives the direction-integrated count rate averaged for all energy and mass channels. The green dashed line denotes the mean value of the background count rate in Sun-oriented, and the green dotted line is three times of background's standard deviations above the green dashed line. (**e**) α_{Sun}. (**f**–**h**) Scatter plots of α_{Sun} versus count rate in the three high count-rate intervals. The gray shaded bars in (**d**–**h**) label the intervals with count rate above the green dotted line. The color bars on top of (**a**) show the spacecraft attitudes in the same format as Figure 3.

To identify intervals of UV contamination, we analyze the direction-integrated count rate of the 8th mass channel, with ion energies averaged over the first four energy channels (2.5–6.4 eV), represented by the red solid curve in Figure 4d. For comparison, we also plot the direction-integrated count rate averaged for all energies and masses (black curve). Magnetosheath ions are discernable in the black curve but negligible in the red curve, where the count rate basically weakly fluctuates around the average (green dashed line in Figure 4d) except during the UV-affected intervals. The exact intervals of UV contamination are identified when the count rates are higher than the average level by at least three standard deviations (derived from the red curve), depicted by the green dotted line in Figure 4d. The three gray shaded bars mark the UV-contaminated intervals. To further investigate the relationship between the UV contamination and the Sun-pointing

direction, we examine scatter plots of the high-count rate versus α_{Sun} in Figure 4f–h. Figure 4h exhibits the α_{Sun}–C_i profile, with a distinguished count rate peak at α_{Sun} = 85.4°. Similarly, the count rates in the two short intervals in Figure 4f, g reach a maximum at around 85°–86°. However, rapid attitude changes (~32 s) during the two short intervals make it difficult to resolve details of the α_{Sun}–C_i profiles. Therefore, we only consider the longer intervals (>160 s) for quantifying the UV contaminations in MINPA.

Based on the analysis, an algorithm is developed to identify UV-contamination intervals in the default mode. First, intervals with count rates exceeding the average background by three standard deviations are elected as UV-contamination candidates. Considering that the background count rate for the whole data set from November 2021 to July 2022 is below $1.5 \times 10^3\ s^{-1}$, a threshold is set to be $2 \times 10^3\ s^{-1}$. Then, candidates with a maximum count rate larger than a threshold are selected. A total of 433 UV-contamination events have been identified by the algorithm from the MINPA default mode ion observations from 13 November 2021 to 31 July 2022. After a manual check, one event is removed from the event set. Among the identified events, 60 long-interval events are found in the Mars-oriented attitude phases, while the rest short-interval events are all identified during rapid maneuver from the Sun-oriented to the Mars-oriented attitude. UV contamination is also observed in the ionosphere mode but is absent in the magnetotail mode. For the ionosphere mode, however, sometimes measurements in the first four energy steps of the heaviest mass channel are mixed with the internal scattering ions, making the identification challenging. Thus, the contamination events in the ionosphere mode are identified manually.

The UV contamination occurrence rate is defined as $\frac{T_{UV}}{T_{op}}$, where T_{op} is the MINPA operation time and T_{UV} is the UV-contaminated duration. The results are summarized in Table 1. From 13 November 2021 to 31 July 2022, the UV-contaminated duration sums up to only 0.9 days, corresponding to a total occurrence rate of 0.48%. This low occurrence rate suggests that the high UV absorption coating [14] used by MINPA effectively suppresses UV contamination, and the majority of MINPA ion observations are free from UV contaminations. In November and December 2021, MINPA most severely suffered from UV contamination, which had occurrence rates of 0.97% and 2.01%, respectively, when the orbit apoapsis was around the south pole. However, due to orbital precession, long-interval events were no longer seen in the Mars-oriented phase after late January 2022, accordingly the occurrence rate of UV contamination was reduced. In June and July 2022, as the orbit apoapsis drifted toward the north pole, the long-interval UV contamination in the default mode reappeared, but at a lower occurrence rate of 0.33%.

Table 1. Occurrence rate of contaminations caused by the solar UV emission to MINPA.

Month	T_{op}	T_{UV}	Ratio
November 2021	12.63	0.12	0.97%
December 2021	22.24	0.45	2.01%
January 2022	23.86	0.05	0.21%
February 2022	21.12	0.04	0.21%
March 2022	21.81	0.04	0.20%
April 2022	22.16	0.03	0.12%
May 2022	22.61	0.03	0.14%
June 2022	20.92	0.07	0.33%
July 2022	20.81	0.07	0.33%
Total	188.17	0.90	0.48%

3.2. Statistical Analysis and UV Path in MINPA

We perform a statistical analysis on 60 long-interval UV-contamination events to examine the accessibility of the solar UV emission to MCPs of MINPA. Figure 5a illustrates

an example of the correlation between the UV-contamination count rate and α_{Sun} observed from 14:18:23 UT to 14:26:52 UT on 02 December 2021. The count rates represent the data obtained from the first four energy channels of the heaviest mass channel, with the average background noise subtracted. Limited by the time resolution (16 s) of MINPA, the peak of the UV contamination may not be fully resolved. Therefore, the data were fitted with a Gaussian distribution to determine the peak location. For the event shown in Figure 5a, the strongest contamination is identified at α_{Sun} = 85.2°, with a full width at half maximum (FWHM) of 1.4°. To define the extent of the contamination, we designate the minimum and maximum values of α_{Sun} as the lower and upper limits, respectively, denoted as α^{l}_{Sun} and α^{u}_{Sun}. For example, in Figure 5a, the UV contamination commences at α^{l}_{Sun} = 83.8° and ends at α^{u}_{Sun} = 86.3°. It is worth noting that the observed profile closely aligns with the fitted curve on the left side, but declines faster than the fitted curve on the right side, suggesting an asymmetric of the UV effect along the polar direction of the instrument.

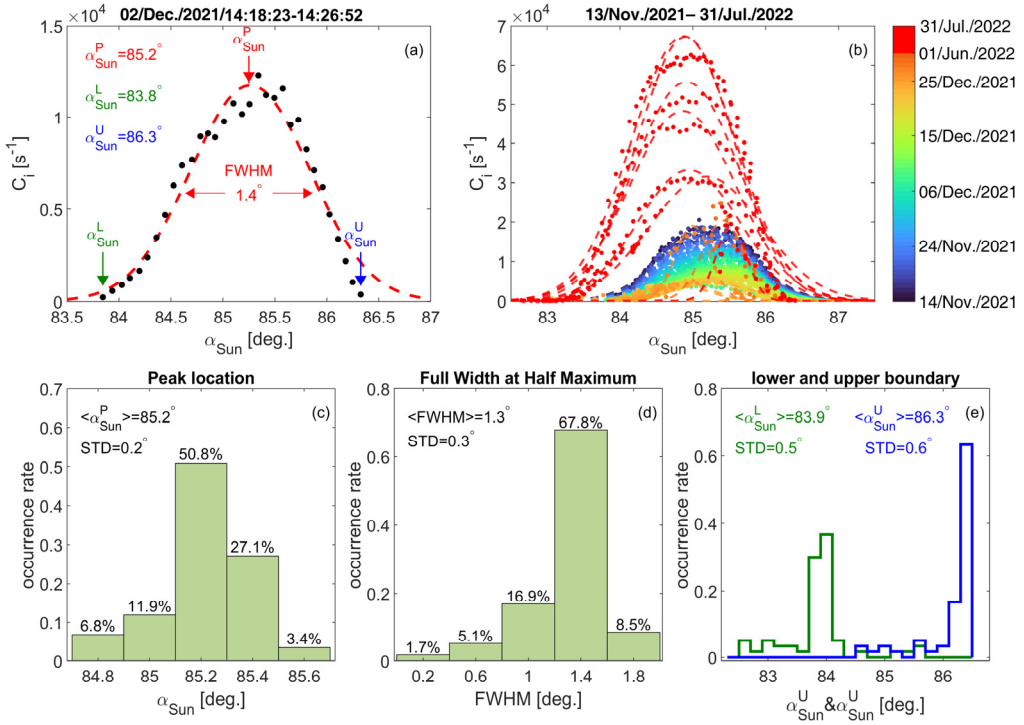

Figure 5. Dependence of UV contamination on α_{Sun}. (**a**) The black dots show an example of UV count rate versus α_{Sun} observed on 02 December 2021. The lower and upper boundary angle (α^{l}_{sun} and α^{u}_{sun}) are 83.8° and 86.3°, respectively. The red dashed curve shows the Gaussian fit, with the peak count rate at α^{p}_{Sun} = 85.2° and the FWHM of 1.4°. (**b**) Statistics of the 60 long-interval UV contaminations from November 2021 to July 2022. Histograms of (**c**) α^{p}_{Sun}, (**d**) FWHM, and (**e**) α^{l}_{sun} and α^{u}_{sun}. The median values and the standard deviations are given in each panel.

Figure 5b displays the count rate profiles of 60 long-interval contaminations, plotted in different colors to distinguish long-interval events observed from November 2021 to January 2022. The count-rate profiles generally exhibit a similar trend. However, it is evident that the magnitudes of UV count rates and the peak locations (α^{p}_{Sun}) vary over time, implying different responses of the azimuth sectors to UV, which will be explored further in the subsequent section. Figure 5c–e present the occurrence rate together with the median values and the standard deviations of α^{p}_{Sun}, FWHM, α^{l}_{Sun} and α^{u}_{Sun}, respectively. In Figure 5c, α^{p}_{Sun} is distributed within a range of 84.8° to 85.6°, with a median value of 85.2° and a standard deviation of 0.2°. Figure 5d illustrates the distribution of FWHM, which ranges between 0.16° and 1.8°. The median value and standard deviation of FWHM are

1.3° and 0.3°, respectively. From Figure 5e, the median values of α^{l}_{Sun} and α^{u}_{Sun} are computed as 83.9° and 86.3°, with the standard deviations of 0.5° and 0.6°, respectively.

Figure 6 presents a cross-sectional view of MINPA. The fact that the UV contamination primarily occurs within the range of 83.9° < α_{Sun} < 86.3° indicates that the contaminations analyzed in this study originate from the UV emission passing through the ENA entrance, as denoted by the red beam in Figure 6. The red arrow denotes the direction of α_{Sun} = 85.2°, which corresponds to the angle where the maximum contamination is typically observed. The asymmetry in the UV-contamination profile (as shown in Figure 5a) may be attributed to the asymmetric internal structure relative to α_{Sun} = 85.2°. Also, it should be noted that the UV emission can also bring high count-rate noise to ENA observations, which will be addressed in future investigations.

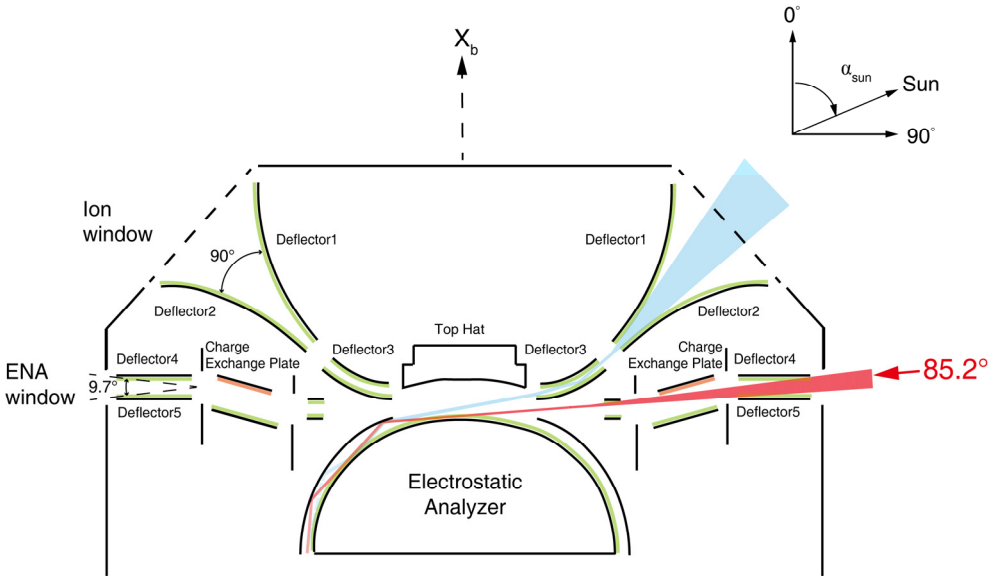

Figure 6. Possible paths of the UV contaminations. The ion and ENA entrances and the outer surface of the inner sphere of ESA are coated (green shaded) to suppress the UV effect. Our analysis reveals that the UV emission can penetrate through the ENA entrances (red beam), leading to high count-rate contamination when α_{Sun} is around 85.2°. Additionally, the UV emission can also pass through the ion entrance (blue beam), contaminating ion and ENA measurements.

3.3. Angular Dependence

MINPA underwent UV calibration using a UV lamp to simulate the Sun in the MEFISTO (MEsskammer für FlugzeitInStrumente und Time-Of-flight) calibration chamber at the University of Bern [14]. The UV source had a central wavelength of 126 ± 5 nm and an intensity of 3.84×10^{13} photons/cm^2/s. To measure the UV responses in all 16 azimuth sectors, calibration was performed approximately every 22.5°. Figure 7a illustrates the normalized UV responses in each azimuth sector, represented by filled circles, along with the corresponding Gaussian profiles (colored curves) fitted to the data. The azimuth sector whose central angle satisfies $|\varphi - \beta_{Sun}| < 11.25°$ is considered to be in the Sun direction. As expected, the ground calibration shows the azimuth sector in the Sun direction has the maximum response when the Sun light irradiates its center. Sectors (1, 8, and 16; 2, 9, and 15 possibly) display lower responses and angular offsets due to partial obstruction caused by the fixture and circuit.

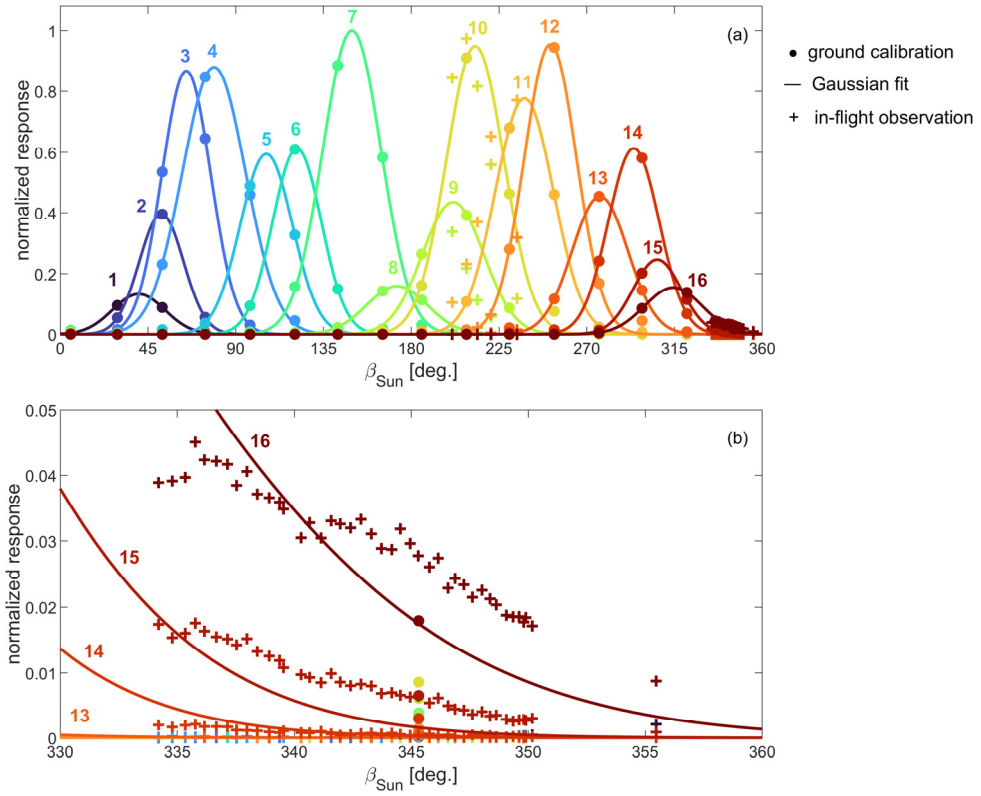

Figure 7. Comparison of the UV responses between ground calibration and in-flight observations. (**a**) UV responses of 16 azimuth sectors from the ground calibration (filled circles) and their Gaussian fittings (curves). The colored crosses denote the normalized UV responses from the in-flight observations from November 2021 to July 2022. (**b**) Zoom-in plot with β_{Sun} from 330° to 360°.

Figure 5b illustrates how the count rates and locations of UV contamination peaks vary with the MINPA operation time. The peak count rates gradually decreased from ~2.1×10^4 s^{-1} to ~2.9×10^3 s^{-1} between November 2021 and January 2022. However, from June to July in 2022, the count rates jumped to a higher level, reaching a maximum around ~6.2×10^4 s^{-1}. These variations are probably attributed to changes in β_{Sun}. When MINPA initiated regular observations in mid-November 2021, β_{Sun} was around 334°, thereafter gradually increased to 360°, then to 45° by January 2022. When the long-interval events reappeared in June and July 2022, β_{Sun} was approximately 220°. To investigate whether the UV count rates correlate with the response of the azimuth sectors, a direct comparison is made between the ground calibration and in-flight observations. Specifically, 47 events within an α_{Sun} coverage of 85.2° ± 1.3°/2 are selected, ensuring that the UV contamination peaks are fully captured by MINPA. The count-rate peaks of the 16 azimuth sectors are scaled to match the ground calibration results and plotted as '+' in Figure 7a. Since the α^{p}_{Sun} (peak location) may slightly differ for different azimuth sectors and the ground calibration is performed at a specific α_{Sun}, different scaling factors are applied to the count-rate peaks measured around β_{Sun}~220° and ~340°, respectively. When β_{Sun}~220°, the in-flight UV contaminations in sectors 9–11 align reasonably well with the ground calibration profiles. Figure 7b is a zoom-in plot from 330° to 360°. The in-flight observations have the same trend as the fitted curves. To sum up, although more observations are needed to show more details about the other sectors, it is reasonable to assume the variations of the UV contamination result from different responses of the azimuth sectors.

The incident UV emission can propagate to the adjacent azimuth sectors due to reflection by the mechanical parts and the top-hat ESA. To identify the azimuth broadening of UV contamination, a criterion is applied: azimuth sectors with count rates within two

orders of magnitude below the maximum are considered to be influenced by the UV emission. Analysis of 47 long-interval events results in the histograms of the azimuth broadening of UV contamination (Figure 8a), from which it is found that 87.6% of the data are UV contaminated, spreading over 3–4 azimuth sectors. The broadening of the UV contamination along the azimuthal direction is associated with the UV responses of the azimuth sectors. Ground calibration forecasts that if the azimuth sectors adjacent to the Sun direction have a higher response, the contamination will be broader.

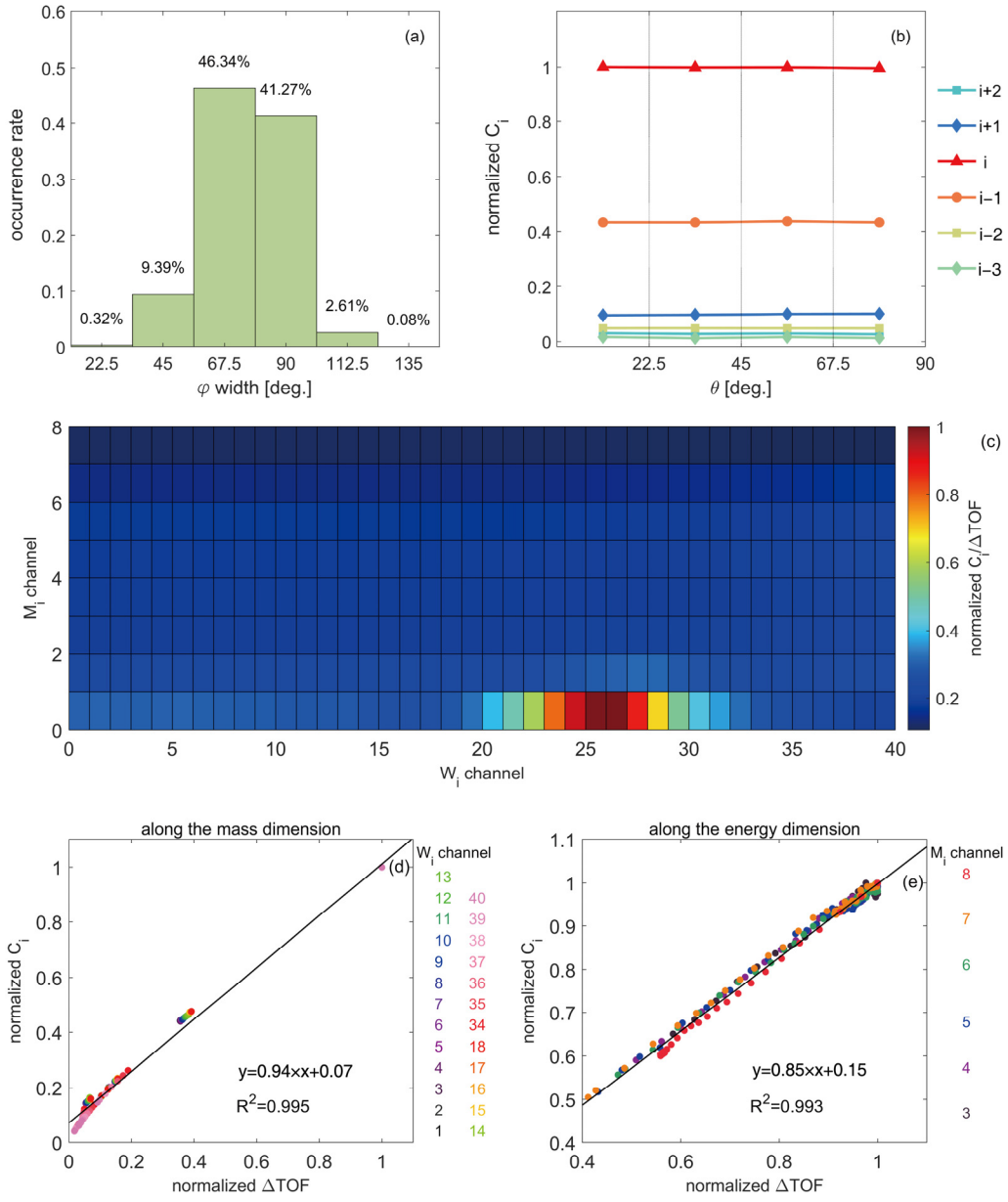

Figure 8. (**a**) Histogram of the azimuthal broadening of UV contamination (φ width). (**b**) Polar angle response to UV contaminations. "i" denotes the azimuthal sector in the Sun direction, and the anticlockwise and clockwise adjacent azimuthal sectors are denoted by "i + j" and "i − j", respectively. (**c**) Normalized count-rate/ΔTOF spectrogram along the mass and energy dimensions and the tick labels of x and y axes represent the number of energy and mass channels, respectively. The red and green rectangles pinpoint the data utilized in (**d**,**e**) panels, respectively. Scatter diagrams of the normalized count rate versus ΔTOF along (**d**) mass dimension, with colors representing the different energy channels, and (**e**) energy dimension with colors representing the different mass channels. The solid lines in (**d**,**e**) are the corresponding linear fittings with equations given in the right bottom corner.

MINPA's polar measurements are achieved by the high voltage applied to the deflectors at the front ion entrance, implying that UV contamination is polar-angle independent. The distribution of UV contamination along the polar angles is shown in Figure 8b. The count rates of the four polar sectors are normalized by the time-averaged maximum value among all contaminated FOVs. The letters "i" and "i ± j" label the azimuthal sector in the Sun direction and the adjacent sectors, where "+" and "-" represent anti-clockwise and clockwise directions, respectively. The data for the i + 3 azimuth sector is not displayed due to lack of samples. As depicted in Figure 8b, the UV contamination is evenly distributed along the polar direction, as expected. Furthermore, it is evident that the azimuth sector in the Sun direction exhibits the strongest contamination, while the contamination in the adjacent sectors decreases significantly, by at least a factor of 2. Combining these findings with the previous results, it can be concluded that approximately one quarter of the 2π FOV is affected by UV contamination, centered at the angular sectors directly exposed to the incident UV emission.

3.4. Mass and Energy Dependence

From Figure 3e,f, it seems that the high masses and energies have high UV-contamination levels. The TOF mass analyzer determines the ion's velocity based on the formula $v = \frac{d}{TOF}$, where TOF represents the time taken to travel the fixed distance d. Then, the ion mass/q can be determined by combining the energy measured by the ESA. However, due to the limitation of resolution, for the given energy, each mass channel corresponds to a broadened TOF, denoted as TOF_1 and TOF_2 (so the TOF table is a matrix with dimension M × E × 2). Given that UV emission cannot be modulated by an electric field, we speculate that the contamination will be homogenous along the TOF. Therefore, it is reasonable to hypothesize that with longer time-of-flight duration, ΔTOF (ΔTOF = $TOF_2 - TOF_1$), more UV counts are accumulated. To verify it, we collect the count rate of the long-interval events from the contaminated angular sectors and present the normalized $C_i/\Delta TOF$ spectrum along the mass and energy dimensions in Figure 8c. High values in the first two mass and the 19th–33rd energy channels come from ambient H^+ and He^{2+} ions in the magnetosheath, ranging from 187 eV to 4.9 keV. Except those ambient signals, the $C_i/\Delta TOF$ values largely remain constant. Further, we extract contaminated count rates and ΔTOF data from each energy channel below 187 eV and above 4.9 keV and normalize them with the maximum in each energy channel, respectively. So, we can focus on the TOF distribution of UV contamination along the mass dimension in each energy channel. Figure 8d illustrates this correlation, with colors representing different energy channels. Linear fitting gives y = 0.94x + 0.07 and a coefficient of determination R^2 = 0.995, indicating a strong linear relationship between the contaminated count rate and ΔTOF in the mass dimension. Similarly, we extract data from the 3rd–7th mass channel separately and the results are shown in Figure 8e in the same format as Figure 8d, with colors representing the different mass channels. Linear fitting gives y = 0.85x + 0.15 and R^2 = 0.993, confirming a high correlation. These analyses confirm that the UV-contaminated count rates vary linearly with ΔTOF along both the mass and energy dimensions.

4. Preliminary Removal of the UV Contaminations

The incident UV emission can interrupt the matching of start and stop signals in the TOF analyzer, leading to a loss of valid signals. Moreover, the incoming UV emission and the ambient ion flux are often aligned, and ion signals can be masked by the noise. To address this issue, we propose a removal algorithm based on the distribution characteristics of UV contamination in phase space to minimize its impact on MINPA's data. First, we determine the noise level caused by UV contamination. We calculate the average count rate of the first four energy sweeps of the heaviest mass channel across the energy and deflection dimensions. This average count rate is then replicated to create a M × E × P × T matrix, which we denote as C_{UV}. Taking into account the correlation between

contaminated count rate in mass-energy dimensions and ΔTOF (see Section 3.3), we determine a mass-energy coefficient (R_1) based on ΔTOF. Multiplying R_1 by C_{UV}, we obtain a noise matrix that is dependent on mass, energy, and azimuth angle. Next, we determine the optimal subtraction ratio based on 320 s normal observations (C_{nor}), 80 s before and after the UV-contamination event. Based on C_{nor}, we calculate the UV noise (C_{sub}) that will be subtracted from the observed data as follows:

$$C_{sub} = \begin{cases} 0 & (R_1 C_{UV} - R_2 C_{nor} \leq 0) \\ R_1 C_{UV} - R_2 C_{nor} & (R_1 C_{UV} - R_2 C_{nor} > 0) \end{cases}, \quad (1)$$

where R_2 is the amplification coefficient determined by the ratio of C_{UV} to the mean value of C_{nor} after excluding data with a count rate $\leq 58.8\ s^{-1}$. Bins that satisfy $R_1 C_{UV} - R_2 C_{nor} \leq 0$ are considered to be valid signals, and no further action is taken for these bins. For the remaining bins, we subtract C_{sub} from the contaminated azimuthal sectors.

Figure 9 is an example of removing the UV contamination by the algorithm. Figure 9a,b display the energy spectrogram of H^+ count rate before and after removal, respectively. We compute the number density and bulk velocity of H^+ to quantitatively evaluate the algorithm. The dashed lines in Figure 9c,d represent the result before removal, which exhibits an abnormal rise in number density and a decrease in bulk velocity in the UV-contaminated interval. As a comparison, the solid lines demonstrate that the plasma moments of H^+ vary smoothly after removal. Figure 9e,g present the count-rate spectrograms of H^+ in the polar-azimuth dimensions observed before (T1), during (T2), and after (T3) the UV contamination. From Figure 9e,g, it can be observed that the incoming ion flows are mainly from 45°–90° of polar angle in the 14th–16th azimuth sectors at T1 and T3. Figure 9f shows that the UV emission incident at 347°, severely affects the 16th azimuth sector and propagates to the adjacent 15th azimuth sector. Apart from the affected 15th–16th azimuth sectors, the count rates in other bins are lower than the observations taken before and after the contamination interval due to the perturbation caused by the UV emission. Figure 9h displays the polar-azimuth spectrogram after removal at T2. In comparison with Figure 9f, a fraction of the count rate is subtracted from the bins outside the main ion incident direction in the affected 15th–16th azimuth sectors. This algorithm performs well in most cases, reducing the UV contamination while maintaining the validity and consistency of the ion data. However, in the boundary layer or regions with sharp plasma gradients, this algorithm may face some difficulties in determining the distribution of valid signals. Nevertheless, it still effectively reduces a significant amount of noise.

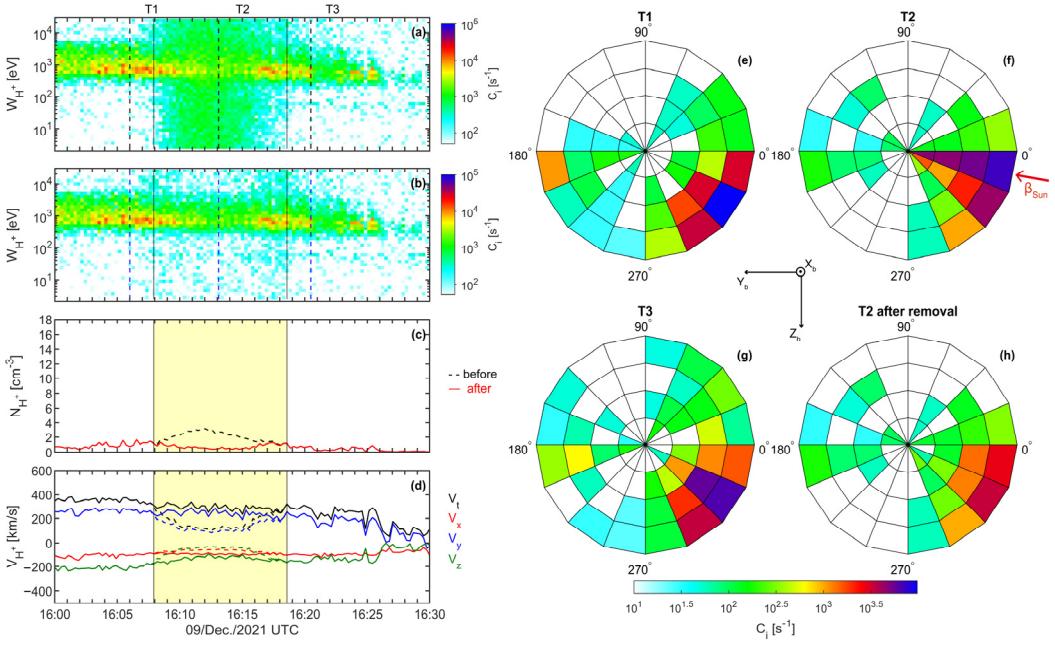

Figure 9. An example of UV-contamination removal. Count-rate spectrograms of (**a**) original H^+ and (**b**) H^+ after removal. (**c**) Number densities of H^+ before (black dashed) and after removal (red solid). (**d**) Bulk velocity of H^+ in the spacecraft coordinates before (dashed) and after removal (solid). The solid vertical lines in (**a**,**b**) and the yellow shades in (**c**,**d**) denote the UV-contaminated interval. (**e**–**g**) Polar and azimuth angle count rate spectrograms of H^+ viewed from $+X_b$ at T1, T2, and T3 times labeled by the vertical dashed lines in (**a**,**b**). (**h**) Count rate spectrogram of H^+ after removal at T2.

5. Discussion and Conclusions

UV contamination is a common issue for space plasma instruments. MINPA, as a standard toroidal top-hat ESA, is susceptible to solar UV emission during in-flight operations. In this study, MINPA's ion observations from November 2021 to July 2022 are fully investigated to characterize the UV contamination. Approximately 0.48% of the ion observations are contaminated by UV emission. It is found that the UV emission primarily enters MINPA through the ENA entrance at α_{sun}~85.2°. The intensity of contamination and its peak location in α_{Sun} vary with β_{Sun} due to variations in the response of different azimuth sectors. The UV contamination can spread to 3–4 azimuth sectors, with the noise primarily centered at the sector in the Sun direction. Since the deflection of ions is determined by the voltage, the UV contamination has a nearly uniform effect on the count rate along the polar dimension. The noise in mass and energy dimensions, on the other hand, is proportional to ΔTOF. Based on these characteristics, we also present a preliminary algorithm to remove the UV noise while preserving the ion signals.

The straight ENA entrance decreases the effectiveness of the coating in suppressing UV contamination. The Neutral Particle Detector (NPD) of the ASPERA-3 instrument on MEX was another victim of UV contamination due to its straight entrance [30]. In contrast, the curved ion entrance achieves good UV suppression as the emission has to undergo multiple reflections at the coated surface before reaching the detector. We observed UV contamination from the ion entrance at a level comparable to the background noise, when α_{Sun} is approximately 35°~50°, as represented by the blue beam in Figure 6. This suggests the necessity for strengthened UV rejection designs at the ENA entrance.

A ground test of the top-hat ESA conducted by Carlson and McFadden [31] indicated that photons predominate over secondary photoelectrons in contamination at energies exceeding 10 eV. As photons are unaffected by the electric field, UV contamination was considered to be energy-independent. In the post-acquisition UV suppression of IMA, a spherical ESA equipped with a circular magnetic velocity analyzer onboard MEX, Fränz et al. [23] treated UV contamination as a uniform background and subtracted a constant count rate from all bins. On the other hand, the distribution of UV contamination was related to the TOF spectrum in the ENA observations carried out by the NPD of ASPERA-3, which utilized a TOF detector to measure the ENA velocity [6,32,33]. It coincides with MINPA observations. The mass and energy dependencies are presumably resulted from the application of the TOF analyzer. Although the energy is determined by the ESA, ions of the same species but with varying energies take different time to traverse the TOF section, leading to different integral times of UV contamination. So, it is necessary to take into account the mass and energy dependencies when addressing noise, such as UV and background noise. Furthermore, if the intensity of UV sources remains relatively constant, the noise signal from UV photons can serve as an indicator of instrument efficiency.

The methods for identifying UV contamination, and the distribution characteristics may give a reference to future missions under UV emission interference. The UV contamination events studied in this paper are considered to be related to the intensity of UV emission, the spacecraft ephemeris, and instrument working modes, which may vary over time. The algorithm developed in this study is just a demonstration for removing UV contamination. To accommodate more scenarios, machine learning may be a good choice in our future studies.

Author Contributions: Conceptualization, L.L. and W.L.; methodology, L.W.; software, J.M. and L.W.; validation, F.Q.; formal analysis, L.W.; investigation, L.W.; resources, A.Z.; data curation, L.K. and Y.Z.; writing—original draft preparation, L.W.; writing—review and editing, L.L., P.W., A.G. and W.L.; visualization, L.W.; supervision, L.L., B.T. and L.X.; project administration, W.L.; funding acquisition, L.L. All authors have read and agreed to the published version of the manuscript.

Funding: This research was funded by the National Natural Science Foundation of China (42241112), the Key Research Program of the Chinese Academy of Sciences (ZDBS-SSW-TLC00103), the National Natural Science Foundation of China (41974170, 42274211), and the Chinese Academy of Sciences (XDB41000000). W. Li and Y. Zhang were supported by the Specialized Research Fund for State Key Laboratories. L. Xie and Y. Zhang were supported by the Youth Innovation Promotion Association of the Chinese Academy of Sciences, and the Pandeng Program of the National Space Science Center, Chinese Academy of Sciences.

Institutional Review Board Statement: Not applicable.

Informed Consent Statement: Not applicable.

Data Availability Statement: The Tianwen-1/MINPA data are available Lunar and Planetary Data Release System (https://moon.bao.ac.cn/web/enmanager/mars1 (accessed on 3 August 2021)). And the MINPA data set we used to create this article is available from the Science Data Bank at https://doi.org/10.57760/sciencedb.space.00907.

Acknowledgments: We acknowledge Tianwen-1 teams for the data and technical support.

Conflicts of Interest: The authors declare no conflict of interest.

References

1. Acuña, M.H.; Connerney, J.E.P.; Wasilewski, P.; Lin, R.P.; Anderson, K.A.; Carlson, C.W.; McFadden, J.; Curtis, D.W.; Mitchell, D.; Reme, H.; et al. Magnetic Field and Plasma Observations at Mars: Initial Results of the Mars Global Surveyor Mission. *Science* **1998**, *279*, 1676–1680. https://doi.org/10.1126/science.279.5357.1676.
2. Acuña, M.H.; Connerney, J.E.P.; Ness, F.N.; Lin, R.P.; Mitchell, D.; Carlson, C.W.; McFadden, J.; Anderson, K.A.; Rème, H.; Mazelle, C.; et al. Global Distribution of Crustal Magnetization Discovered by the Mars Global Surveyor MAG/ER Experiment. *Science* **1999**, *284*, 790–793. https://doi.org/10.1126/science.284.5415.790.
3. Lundin, R.; Barabash, S.; Andersson, H.; Holmström, M.; Grigoriev, A.; Yamauchi, M.; Sauvaud, J.-A.; Fedorov, A.; Budnik, E.; Thocaven, J.-J.; et al. Solar Wind-Induced Atmospheric Erosion at Mars: First Results from ASPERA-3 on Mars Express. *Science* **2004**, *305*, 1933–1936. https://doi.org/10.1126/science.1101860.
4. Dong, Y.; Fang, X.; Brain, D.A.; McFadden, J.P.; Halekas, J.S.; Connerney, J.E.; Curry, S.M.; Harada, Y.; Luhmann, J.G.; Jakosky, B.M. Strong plume fluxes at Mars observed by MAVEN: An important planetary ion escape channel. *Geophys. Res. Lett.* **2015**, *42*, 8942–8950. https://doi.org/10.1002/2015gl065346.
5. Halekas, J.S.; Brain, D.A.; Ruhunusiri, S.; McFadden, J.P.; Mitchell, D.L.; Mazelle, C.; Connerney, J.E.P.; Harada, Y.; Hara, T.; Espley, J.R.; et al. Plasma clouds and snowplows: Bulk plasma escape from Mars observed by MAVEN. *Geophys. Res. Lett.* **2016**, *43*, 1426–1434. https://doi.org/10.1002/2016gl067752.
6. Futaana, Y.; Barabash, S.; Grigoriev, A.; Holmström, M.; Kallio, E.; Brandt, P.C.s.; Gunell, H.; Brinkfeldt, K.; Lundin, R.; Andersson, H.; et al. First ENA observations at Mars: Subsolar ENA jet. *Icarus* **2006**, *182*, 413–423. https://doi.org/10.1016/j.icarus.2005.08.024.
7. Futaana, Y.; Chaufray, J.-Y.; Smith, H.T.; Garnier, P.; Lichtenegger, H.; Delva, M.; Gröller, H.; Mura, A. Exospheres and Energetic Neutral Atoms of Mars, Venus and Titan. *Space Sci. Rev.* **2011**, *162*, 213–266. https://doi.org/10.1007/s11214-011-9834-4.
8. Galli, A.; Wurz, P.; Barabash, S.; Grigoriev, A.; Gunell, H.; Lundin, R.; Holmström, M.; Fedorov, A. Energetic Hydrogen and Oxygen Atoms Observed on the Nightside of Mars. *Space Sci. Rev.* **2006**, *126*, 267–297. https://doi.org/10.1007/s11214-006-9088-8.
9. Rème, H.; Bosqued, J.M.; Sauvaud, J.A.; Cros, A.; Dandouras, J.; Aoustin, C.; Bouyssou, J.; Camus, T.; Cuvilo, J.; Martz, C.; et al. The Cluster Ion Spectrometry(CIS) Experiment. *Space Sci. Rev.* **1997**, *79*, 303–350. https://doi.org/10.1023/a:1004929816409.
10. McComas, D.J.; Bame, S.J.; Barker, P.; Feldman, W.C.; Phillips, J.L.; Riley, P.; Griffee, J.W. *Solar Wind Electron Proton Alpha Monitor (SWEPAM) for the Advanced Composition Explorer*; Springer, Dordrecht, 1998; pp. 563–612.
11. Jakosky, B.M.; Lin, R.P.; Grebowsky, J.M.; Luhmann, J.G.; Mitchell, D.F.; Beutelschies, G.; Priser, T.; Acuna, M.; Andersson, L.; Baird, D.; et al. The Mars Atmosphere and Volatile Evolution (MAVEN) Mission. *Space Sci. Rev.* **2015**, *195*, 3–48. https://doi.org/10.1007/s11214-015-0139-x.
12. Cara, A.; Lavraud, B.; Fedorov, A.; De Keyser, J.; Demarco, R.; Marcucci, M.F.; Valentini, F.; Servidio, S.; Bruno, R. Electrostatic analyzer design for solar wind proton measurements with high temporal, energy, and angular resolutions. *J. Geophys. Res. Space Phys.* **2017**, *122*, 1439–1450. https://doi.org/10.1002/2016ja023269.

13. Zou, Y.; Zhu, Y.; Bai, Y.; Wang, L.; Jia, Y.; Shen, W.; Fan, Y.; Liu, Y.; Wang, C.; Zhang, A.; et al. Scientific objectives and payloads of Tianwen-1, China's first Mars exploration mission. *Adv. Space Res.* **2021**, *67*, 812–823. https://doi.org/10.1016/j.asr.2020.11.005.
14. Kong, L.; Zhang, A.; Tian, Z.; Zheng, X.; Wang, W.; Liu, B.; Wurz, P.; Piazza, D.; Etter, A.; Su, B.; et al. Mars Ion and Neutral Particle Analyzer (MINPA) for Chinese Mars Exploration Mission (Tianwen-1): Design and ground calibration. *Earth Planet. Phys.* **2020**, *4*, 333–344. https://doi.org/10.26464/epp2020053.
15. Carlson, C.W.; Curtis, D.W.; Paschmann, G.; Michel, W. An instrument for rapidly measuring plasma distribution functions with high resolution. *Adv. Space Res.* **1982**, *2*, 67–70. https://doi.org/10.1016/0273-1177(82)90151-X.
16. Barabash, S.; Lundin, R.; Andersson, H.; Brinkfeldt, K.; Grigoriev, A.; Gunell, H.; Holmström, M.; Yamauchi, M.; Asamura, K.; Bochsler, P.; et al. The Analyzer of Space Plasmas and Energetic Atoms (ASPERA-3) for the Mars Express Mission. *Space Sci. Rev.* **2006**, *126*, 113–164. https://doi.org/10.1007/s11214-006-9124-8.
17. Halekas, J.S.; Taylor, E.R.; Dalton, G.; Johnson, G.; Curtis, D.W.; McFadden, J.P.; Mitchell, D.L.; Lin, R.P.; Jakosky, B.M. The Solar Wind Ion Analyzer for MAVEN. *Space Sci. Rev.* **2015**, *195*, 125–151. https://doi.org/10.1007/s11214-013-0029-z.
18. McFadden, J.P.; Kortmann, O.; Curtis, D.; Dalton, G.; Johnson, G.; Abiad, R.; Sterling, R.; Hatch, K.; Berg, P.; Tiu, C.; et al. MAVEN SupraThermal and Thermal Ion Compostion (STATIC) Instrument. *Space Sci. Rev.* **2015**, *195*, 199–256. https://doi.org/10.1007/s11214-015-0175-6.
19. Gloeckler, G. Ion composition measurement techniques for space plasmas. *Rev. Sci. Instrum.* **1990**, *61*, 3613–3620. https://doi.org/10.1063/1.1141581.
20. Morel, X.; Berthomier, M.; Berthelier, J.J. Electrostatic analyzer with a 3-D instantaneous field of view for fast measurements of plasma distribution functions in space. *J. Geophys. Res. Space Phys.* **2017**, *122*, 3397–3410. https://doi.org/10.1002/2016ja023596.
21. Alsop, C.; Scott, S.; Free, L. UV Rejection Design and Performance of the PEACE Electrostatic Analyzers. In *Measurement Techniques in Space Plasmas: Particles*; American Geophysical Union: Washington, DC, USA, 1998; pp. 269–274.
22. Eparvier, F.G.; Chamberlin, P.C.; Woods, T.N.; Thiemann, E.M.B. The Solar Extreme Ultraviolet Monitor for MAVEN. *Space Sci. Rev.* **2015**, *195*, 293–301. https://doi.org/10.1007/s11214-015-0195-2.
23. Fränz, M.; Dubinin, E.; Roussos, E.; Woch, J.; Winningham, J.D.; Frahm, R.; Coates, A.J.; Fedorov, A.; Barabash, S.; Lundin, R. Plasma Moments in the Environment of Mars. *Space Sci. Rev.* **2006**, *126*, 165–207. https://doi.org/10.1007/s11214-006-9115-9.
24. Nozzoli, F.; Richelli, P. Moon Mapping Project Results on Solar Wind Ion Flux and Composition. *Universe* **2021**, *7*, 157. https://doi.org/10.3390/universe7050157.
25. Zhang, A.; Kong, L.; Li, W.; Li, L.; Tang, B.; Rong, Z.; Wei, Y.; Ma, J.; Zhang, Y.; Xie, L.; et al. Tianwen-1 MINPA observations in the solar wind. *Earth Planet. Phys.* **2022**, *6*, 1–9. https://doi.org/10.26464/epp2022014.
26. Fan, K.; Yan, L.; Wei, Y.; Zhang, A.; Kong, L.; Fränz, M.; He, F.; Chai, L.; Yuan, C.; Wang, Y.; et al. The solar wind plasma upstream of Mars observed by Tianwen-1: Comparison with Mars Express and MAVEN. *Sci. China Earth Sci.* **2022**, *65*, 759–768. https://doi.org/10.1007/s11430-021-9917-0.
27. Wang, J.; Shi, Y.; Luo, B.; Liu, S.; Kong, L.; Ma, J.; Li, W.; Tang, B.; Zhang, A.; Li, L.; et al. Upstream Solar Wind Prediction up to Mars by an Operational Solar Wind Prediction System. *Space Weather.* **2023**, *21*, e2022SW003281. https://doi.org/10.1029/2022sw003281.
28. Trotignon, J.G.; Mazelle, C.; Bertucci, C.; Acuña, M.H. Martian shock and magnetic pile-up boundary positions and shapes determined from the Phobos 2 and Mars Global Surveyor data sets. *Planet. Space Sci.* **2006**, *54*, 357–369. https://doi.org/10.1016/j.pss.2006.01.003.
29. Young, D.T.; Berthelier, J.J.; Blanc, M.; Burch, J.L.; Coates, A.J.; Goldstein, R.; Grande, M.; Hill, T.W.; Johnson, R.E.; Kelha, V.; et al. Cassini Plasma Spectrometer Investigation. *Space Sci. Rev.* **2004**, *114*, 1–112. https://doi.org/10.1007/s11214-004-1406-4.
30. Wüest, M.; Evans, D.; von Steiger, R. *Calibration of Particle Instruments in Space Physics*; ESA Publications Division: Noordwijk, The Netherlands, 2007; pp. 294–295.
31. Carlson, C.W.; McFadden, J.P. Design and Application of Imaging Plasma Instruments. In *Measurement Techniques in Space Plasmas: Particles*; American Geophysical Union: Washington, DC, USA, 1998; pp. 125–140.
32. Galli, A.; Wurz, P.; Lammer, H.; Lichtenegger, H.I.M.; Lundin, R.; Barabash, S.; Grigoriev, A.; Holmström, M.; Gunell, H. The Hydrogen Exospheric Density Profile Measured with ASPERA-3/NPD. *Space Sci. Rev.* **2006**, *126*, 447–467. https://doi.org/10.1007/s11214-006-9089-7.
33. Mura, A.; Orsini, S.; Milillo, A.; Kallio, E.; Galli, A.; Barabash, S.; Wurz, P.; Grigoriev, A.; Futaana, Y.; Andersson, H.; et al. ENA detection in the dayside of Mars: ASPERA-3 NPD statistical study. *Planet. Space Sci.* **2008**, *56*, 840–845. https://doi.org/10.1016/j.pss.2007.12.013.